ACS APPLIED NANO MATERIALS

www.acsanm.org Article

Pt Nanoparticles Supported on a Mesoporous (La,Sr)(Ti,Fe)$O_{3-\delta}$ Solid Solution for the Catalytic Oxidation of CO and CH_4

Buğra Kayaalp,[⊥] Siwon Lee,[⊥] Luca Nodari, Jongsu Seo, Seunghyun Kim, WooChul Jung,* and Simone Mascotto*

Cite This: *ACS Appl. Nano Mater.* 2020, 3, 11352−11362 Read Online

ACCESS | Metrics & More | Article Recommendations | Supporting Information

ABSTRACT: The synthesis of a mesoporous (La,Sr)(Ti,Fe)$O_{3-\delta}$ (LSTF) solid solution and its application as a catalytic support is presented. A mesoporous nanostructured perovskite solid solution with a tunable specific surface area and pore volume of up to 201 $m^2\ g^{-1}$ and 0.411 $cm^3\ g^{-1}$, respectively, was obtained by a sol−gel-like SiO_2 endotemplating approach. Very high porosity combined with the redox-active characteristics of the perovskite structure makes these systems effective supports for Pt nanoparticle (NP) catalysts. As a result, when 0.8 wt % Pt NPs was introduced, the mesoporous LSTF showed improved CO and CH_4 oxidation rates compared to commercially available SiO_2 or CeO_2. These observations demonstrate the promotional effects between Pt and LSTF and suggest an efficient strategy for achieving active support materials toward oxidation catalysis.

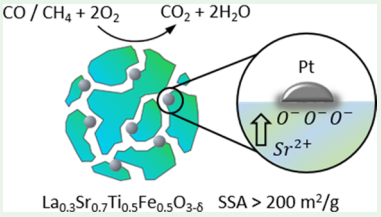

KEYWORDS: *mesoporous perovskite, metal−support interactions, surface segregation, surface reconstruction, volatile organic compounds*

INTRODUCTION

The interest in cost-effective, reactive, and stable catalysts for the complete oxidation of CO and hydrocarbon fuels is growing each year due to the demand for efficient power generation and pollution-abatement systems.[1] Supported noble metals, which combine the superior activity of noble-metal nanoparticles (NPs) with the stability and cost effectiveness of oxide supports, are currently employed as industry-standard catalytic systems. Metal−support interactions in these systems usually lead to a dramatic improvement of the catalytic properties from both standalone constituents, i.e., noble-metal nanoparticles and the reducible oxide.[2−5] Improved reactivity due to the electronic and ionic charge carrier transfer between the metal and support,[5−9] stabilization of the oxidation state of the active phase,[8,10−13] and sintering resistance[14−17] are reported for numerous supported metal catalysts.

Transition-metal oxide supports, which have high conductivity for oxygen ions, readily supply oxygen to the active phase and rapidly exchange oxygen from or to surrounding gases.[18−20] The oxygen supply/exchange capability becomes particularly crucial when the material is used in applications, such as exhaust catalysis, where atmospheric oxygen can be scarce during catalytic operation and lattice oxygen from the support should actively participate in the oxidation reaction.[7,21] Moreover, the presence of mixed conductivity allows the support to be used directly as an electrode in electrochemical devices. Within the class of transition-metal oxide materials, perovskite oxide is particularly promising candidates to implement as active supports due to their compositional flexibility, high stability, and oxygen storage capability.[22−24] Moreover, in comparison with commonly used CeO_2-based supports, several nanoscaled perovskite oxide compositions show superior standalone hydrocarbon oxidation activity and thermal stability at lower material costs.[25,26]

Besides their chemical nature, the design of nanostructured active supports is extremely beneficial for the further improvement of catalytic performance.[5,27−30] In particular, nanoporous supports enable superior dispersion and reactivity of the active phase,[30] a percolated structure for an improved contact area, easy access of reactants,[31,32] and resistance to deactivation.[16,33]

For these reasons, intensive research has been dedicated over the past few years to the use of mesoporous structures in heterogeneous catalysis applications. After the pioneering work of Ryoo et al.,[34,35] groups led by de Jong and de Jongh engaged in consistent work on the synthesis, characterization, and catalytic efficiency of metal nanoparticles supported on nanoporous ordered SiO_2.[16,36,3716,36,37] Quite recently, they showed that silica supports with specific mesoporous sizes are the main factors affecting the stability of the metal nanoparticle catalysts by controlling their diffusion and coalescence.[38] In another study, the spatial distribution of metal nanoparticle catalysts as a function of the mesopore size of the SiO_2 substrate was discussed.[39] Growth and deactivation of Cu

Received: September 9, 2020
Accepted: October 29, 2020
Published: November 12, 2020

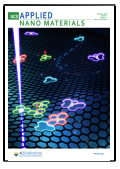

https://dx.doi.org/10.1021/acsanm.0c02456
ACS Appl. Nano Mater. 2020, 3, 11352−11362

Scheme 1. Representation of the Synthesis Procedure of the Mesoporous (La,Sr)(Ti,Fe)$O_{3-\delta}$ Solid Solution (Blue-Green) via the Silica Endotemplating Method (Yellow) and Pt Nanoparticle (Gray) Deposition through the Electrostatic Attraction between Pt and the LSTF Support

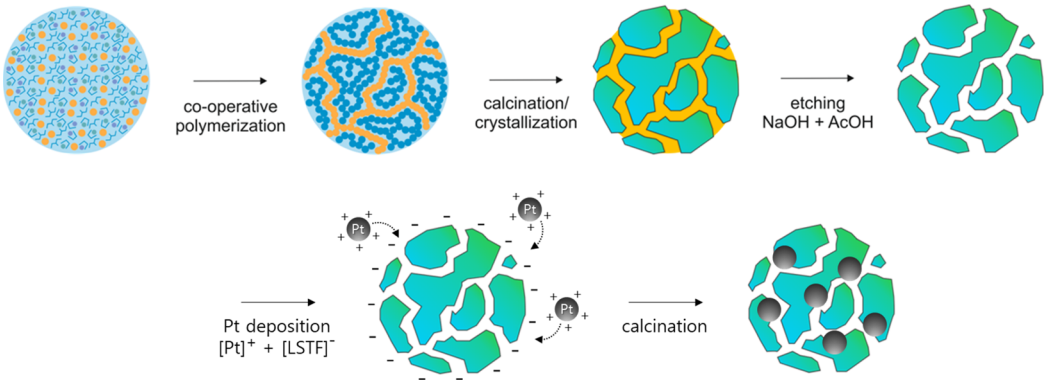

nanoparticles grown inside substrate cavities were found to depend directly on the pore size of the oxide.

The upcoming development step with regard to catalysis substrate designs would be the preparation of mesoporous mixed ion-electron conductor (MIEC) materials, thus combining the aforementioned high surface reactivity with the benefits of a mesoporous oxide structure. The preparation of nanoporous MIEC materials is, however, highly challenging, especially when attempted with perovskite family materials. The main issue lies in the high temperatures (T > 600 °C) required for the perovskite system to crystallize, as these temperatures are much higher than the combustion temperature of standard organic pore templates, inevitably leading to pore collapse.

In addition to the nanocasting approach,[40,41] the development of alternative, more rapid synthesis strategies for mesoporous perovskite oxides has become necessary. Previously, we reported the preparation of mesoporous nanostructured $SrTiO_3$ and (La,Sr)(Ti,Fe)$O_{3-\delta}$ (LSTF) solid solutions using a hard endotemplate[42] and a template-free route,[43] respectively. Herein, we present the synthesis of mesoporous LSTF materials with a much greater degree of porosity and assess their functional properties as metal catalyst supports for low- and high-temperature oxidation catalysis. The use of a nanostructured siliceous endotemplate phase obtained by a sol−gel reaction in a reaction mixture (Scheme 1) engendered mesoporous perovskite structures with a tunable specific surface area and pore volume as well as substantial high-temperature stability. The increased nanoporosity combined with the intrinsic redox characteristics of the oxide matrix promoted strong interactions with noble-metal catalysts, allowing the prepared systems to outperform standard SiO_2 or CeO_2 support materials for CO and CH_4 oxidation. Moreover, the nanoporous LSTF solid solutions can also serve as standalone catalysts, showing potential as substitutional materials for noble-metal catalysts.

EXPERIMENTAL SECTION

Reagents. Strontium nitrate (99%, Acros Organics), titanium (IV) isopropoxide (98%, ABCR), iron (III) nitrate nonahydrate (reagent grade, Merck), lanthanum (III) nitrate hexahydrate (99.9%, Alfa Aesar), tetraethyl orthosilicate (TEOS) (98%, Alfa Aesar), anhydrous citric acid (99.6%, Acros Organics), hydrochloric acid (37%, VWR), ethanol (99.8%, VWR), glycerol (99%, Alfa Aesar), glacial acetic acid (HOAc 99%, VWR), potassium tetrachloroplatinate (II) (K_2PtCl_4, 99.9%, Pt 46.0%, Alfa Aesar), trimethyloctadecylammonium bromide ($C_{21}H_{46}BrN$, 98%, Sigma-Aldrich), sodium borohydride ($NaBH_4$, 98%, Alfa Aesar), ammonia solution (NH_3, 28−30 wt %, Junsei Chemical), and cerium nitrate hexahydrate ($Ce(NO_3)_3{\cdot}6H_2O$, 99.99%, Alfa Aesar) were used as received without further purification.

Synthesis of Mesoporous LSTF. Highly porous LSTF solid solutions with the $La_{0.3}Sr_{0.7}Ti_{0.5}Fe_{0.5}O_{3-\delta}$ nominal stoichiometry were prepared by a coassembly approach using the polymer complex route. The preparation of the prehydrolyzed TEOS solution is described in the literature.[42] In a typical synthesis, 5.43 mmol titanium (IV) isopropoxide was added to 11.9 mL of glycerol. After 30 min of stirring, 40.7 mmol citric acid was added. The reaction mixture was heated to 60 °C and stirred until the complete dissolution of the citric acid. Subsequently, $Sr(NO_3)_2$ at 3.80 mmol was dissolved in 1.0 mL of deionized water, and 1.63 mmol $La(NO_3)_3{\cdot}6H_2O$ and 2.72 mmol $Fe(NO_3)_3{\cdot}9H_2O$ were added at 30 min intervals under stirring. The silica source was then introduced into the mixture to reach a SiO_2/LSTF nanocomposite molar ratio between 0.2 and 1.0, corresponding to volume fractions between 10 and 40 vol %. The volume fraction values were calculated using a value of 5.62 g cm^{-3} for fully dense $La_{0.3}Sr_{0.7}Ti_{0.5}Fe_{0.5}O_{3-\delta}$ (see the Supporting Information for density calculations). After equilibration for another 1.5 h, the temperature of the mixture was increased to 130 °C. The polymerization between the chelating agents occurred under strong stirring for 2 h. The resulting gel was annealed in air with a heating ramp of 2 °C min^{-1}. A dwell time of 2 h was then set both at the intermediate and final temperature steps of 400 and 600 °C, respectively. The obtained SiO_2/LSTF material was then treated with glacial acetic acid (1.0 mM) to get rid of carbonate impurities.[43,44] Removal of the SiO_2 phase was achieved by an etching treatment with 2 M NaOH at 90 °C for 24 h. Finally, the acetic acid washing step was repeated. Subsequent to each step, the materials were thoroughly washed with deionized water to ensure pH-neutrality. The samples were labeled based on their initial template loading level as LSTF-10, LSTF-20, and LSTF-40 for 10, 20, and 40 vol % respectively.

Synthesis and Deposition of Pt Nanoparticles. Potassium tetrachloroplatinate (10 mM, 5 mL) and trimethyloctadecylammonium bromide (400 mM, 12.5 mL) aqueous solutions were blended with 29.5 mL of DI water, and the mixture was heated to 55 °C for 25 min. Subsequently, an aqueous solution of sodium borohydride (500 mM, 3 mL) was added to the mixture solution. The hydrogen gas generated inside the flask was released for 20 min through a syringe needle. Afterward, the mixture was aged at 55 °C for 15 h under magnetic stirring. The final brown solution was mixed with 10 mL of ethanol and centrifuged at 12 000 rpm for 60 min. After removing the supernatant solution and replacing that amount with DI water, the mixture solution was centrifuged at 12 000 rpm for 60 min again. The collected precipitates were then dispersed in 5 mL of DI water for further use.

https://dx.doi.org/10.1021/acsanm.0c02456
ACS Appl. Nano Mater. 2020, 3, 11352−11362

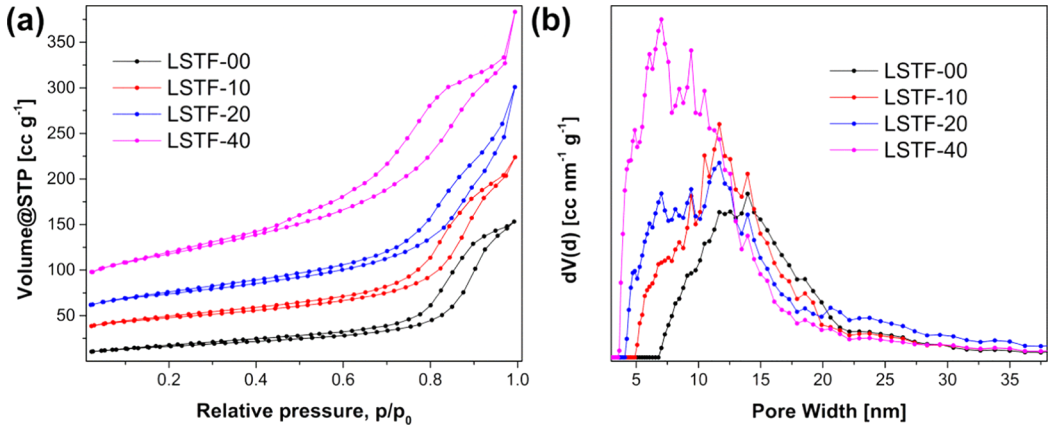

Figure 1. Nitrogen physisorption isotherms: (a) pore size distribution (b) of the LSTF samples. Isotherms of LSTF-00 were retrieved from earlier work.[43] The isotherms were each separated by a 20 $cm^3\ g^{-1}$ offset for clarity.

To prepare Pt NPs supported on the highly porous LSTF-40, CeO_2, and SiO_2, each oxide powder was initially dispersed in 100 mL of water at pH 10. Modification with a basic solution was done to achieve a negative surface charge for the oxide.[45−47] The porous CeO_2 support was synthesized by the calcination of cerium nitrate hexahydrate at 450 °C for 20 h in air. The specific surface area was 72.2 $m^2\ g^{-1}$ (Figure S1) and was similar to those of supports prepared by the wash-coating method in the literature.[48,49] For the SiO_2 support, we used a commercialized material (silicon (IV) oxide nanopowder, 80 nm ammonium persulfate (APS) powder). The as-prepared Pt NPs (561.8 ppm), surrounded by cationic surfactants and positively charged,[15,50,51] were then mixed with the negatively charged oxide support under stirring at 300 rpm for 10 min to prepare Pt (0.8 wt %)/oxide support catalysts. The final suspension was centrifuged at 8000 rpm for 10 min and the collected precipitates were dried at 80 °C overnight in an oven. The as-synthesized Pt (0.8 wt %)/oxide support catalysts were calcined at 350 °C for 5 h in air.

X-ray Diffraction. X-ray diffraction (XRD) studies were performed using an X'Pert Pro diffractometer (PANalytical Corp.) with 1.5406 Å Ni-filtered Cu Kα radiation operating at 45 kV and 40 mA. The average size of crystallites was obtained from the full width at half-maximum (FWHM) of the (110) reflection using the Scherrer formula.

Mössbauer Spectroscopy. Mössbauer spectroscopy was performed at room temperature on a constant acceleration spectrometer with a mounted Rh matrix 57Co source at a nominal strength of 1850 MBq. A detailed description of the hyperfine parameters is reported in Table S1. Lorentzian line shapes with the minimum number of components were used to fit the spectra. δ is quoted relative to a standard α-Fe foil.

Nitrogen Physisorption. A Quadrasorb SI-MP gas physisorption setup by Quantachrome was used to perform nitrogen physisorption measurements at the gas boiling temperature. The samples were previously outgassed with a Masterprep Degasser (Quantachrome Corp.) for 12 h at 120 °C. The material specific surface areas were obtained using the Brunauer−Emmett−Teller (BET) method[52] in the relative pressure range 0.07−0.3. The pore size distribution was calculated using Quantachrome ASiQWin software and applying the nonlocal density functional theory (NLDFT) method[53] for cylindrical pores on the isotherm adsorption branch.

Temperature-Programmed Reduction of H_2 (H_2-TPR). Temperature-programmed reduction experiments were carried out with hydrogen using a Micromeritics AutoChem 2920 apparatus. Each sample (~45 mg) was pretreated at 550 °C for 2 h in an oxygen atmosphere (5% O_2). After the pretreatment, each was cooled to 50 °C. Then, a 5% H_2−He mixture (50 mL min^{-1}) was introduced into the sample and the temperature was ramped to 600 °C (10 °C min^{-1}). The signal for H_2 consumption was recorded by a thermal conductivity detector (TCD).

Electron Microscopy. Transmission electron microscopy (TEM) analyses were performed on a JEOL JEM 2200 FS operating at 200 kV mounting two CEOS Cs correctors (CETCOR, CESCOR), a JEOL JED-2300 Si(Li) energy-dispersive X-ray spectroscopy (EDX) detector, a Gatan 4K UltraScan 1000 camera, and a high-angle annular dark-field (HAADF) detector. Regarding the sample preparation, the material was ground into a fine powder and later suspended in toluene by sonication. Finally, the suspension was dropped onto a carbon-coated 400 mesh TEM grid and the solvent in excess was removed by drying under air.

EDX mapping analyses were collected using 256 × 256 pixels (pixel size of 0.7 nm) and a dwell time of 0.5 ms $pixel^{-1}$ (corrected for dead time) with 30 cycles. For the sake of reproducibility, EDX measurements were repeated on three positions for each sample. The surveyed cations showed less than 1.0 atom % disparity at each point.

CH_4 and CO Oxidation Tests. A lab-scale fixed-bed reactor (4 mm inner diameter) was used to undertake the catalytic activity measurement test for CH_4 and CO oxidation. For each test, 100 mg of the catalyst was mixed with quartz sand (100 mg, 50−70 mesh particle size) and the mixture was loaded between quartz wool layers to prevent the displacement of the catalyst (Figure S2). The quartz sand was mixed with the catalyst to minimize the thermal gradient inside the catalytic bed and to prevent the blockage of the gas flow, which may arise due to the close-packed nanocatalysts in the reactor. For methane oxidation, the reactant consisted of 2 vol % CH_4 and 4 vol % O_2 balanced in Ar. The feed stream for carbon monoxide oxidation was composed of 1 vol % CO and 4 vol % O_2 balanced in Ar. The gas flow rate for both reactions was held at 50 mL min^{-1}, corresponding to a weight hourly space velocity (WHSV) of 30 000 mL $g_{catal}^{-1}\ h^{-1}$. The outlet gases were detected using a mass spectrometer (PFEIFFER Vacuum GSD320) in real time. After activating the catalyst in the reaction environment at 600 and 300 °C for CH_4 and CO oxidation, respectively, the light-off curve for each catalyst was plotted under continuous ramping of the temperature (3 °C min^{-1}). The conversion ratio (%) is defined as the ratio of the converted gas to the total input gas and is expressed as the following equations.

$$CH_4\ \text{conversion ratio}(\%) = \frac{\text{mol}_{CH_4,\text{inlet}} - \text{mol}_{CH_4,\text{outlet}}}{\text{mol}_{CH_4,\text{inlet}}} \times 100$$

$$\text{CO conversion ratio}(\%) = \frac{\text{mol}_{CO,\text{inlet}} - \text{mol}_{CO,\text{outlet}}}{\text{mol}_{CO,\text{inlet}}} \times 100$$

Reaction orders for CH_4 and O_2 were determined by switching the partial pressures of CH_4 (from 2×10^{-3} to 6×10^{-3} atm) and O_2 (from 1×10^{-2} to 5×10^{-2} atm) at the corresponding fixed partial pressures of 5×10^{-2} and 2×10^{-3} atm for O_2 and CH_4. In a similar manner, for the reaction orders for CO and O_2, we varied the partial

https://dx.doi.org/10.1021/acsanm.0c02456
ACS Appl. Nano Mater. 2020, 3, 11352−11362

Table 1. Crystallite Sizes (Φ) Retrieved from XRD, Specific Surface Area (S_{BET}), and Pore Volume (V_P) Determined by N_2 Physisorption, Average Atomic Composition of the Elements Determined by EDX (Atom % Values Normalized by the Total Nominal Cation Amount in the $La_{0.3}Sr_{0.7}Ti_{0.5}Fe_{0.5}O_{3-\delta}$ Molecular Formula), and Compositions of Different Fe Sites Retrieved by Mössbauer Spectroscopy for the Investigated LSTF Oxides[a]

sample code	template loading [vol %]	Φ [nm]	S_{BET} [$m^2 g^{-1}$]	V_P [$cm^3 g^{-1}$]	La/Sr atomic ratio	Fe/Ti atomic ratio	Fe^{3+} (1) [%]	Fe^{3+} (2) [%]	Fe^{3+} (3) [%]	Fe^{4+} [%]
LSTF-00		22	60	0.24	0.42	0.96	60	30		10
LSTF-10	10	20	98	0.29	0.47	0.9	33	41	19	7
LSTF-20	20	19	125	0.34	0.45	0.68	33	46	16	5
LSTF-40	40	18	201	0.41	0.64	0.58	23	32	38	7

[a]The parameters for the template-free material (LSTF-00) were taken from the literature.[43]

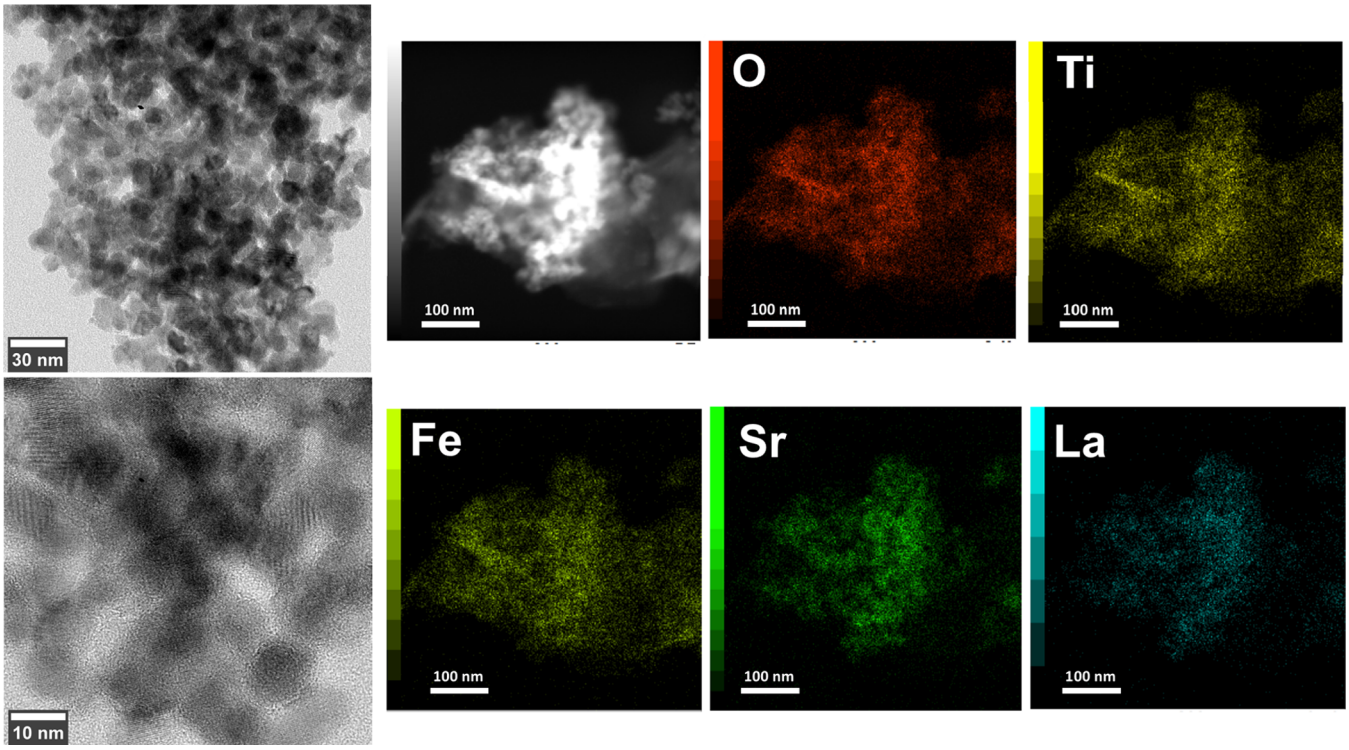

Figure 2. HR-TEM images and EDX mapping images of LSTF-40 chosen as a representative system.

pressures of CO (from 1×10^{-3} to 5×10^{-3} atm) and O_2 (from 1×10^{-2} to 5×10^{-2} atm) while keeping the corresponding partial pressures of O_2 (5×10^{-2} atm) and CO (1×10^{-3} atm) constant. To monitor the signal for CH_4, we used the peak at $m/z = 15$ instead of that at 16, thereby excluding the interference from CO, CO_2, H_2O, and O_2 species. The signal for CO was corrected considering the contribution from CO_2 via the mass concentration determination (MCD) mode.

Thermal Analysis. The material thermal stability under different atmosphere conditions was tested using a NETZSCH STA 449F3 thermobalance connected with a capillary to an Aëolos QMS403C mass spectrometer device. Under a reducing atmosphere, samples were treated by ramping at 5 °C min^{-1} up to 600 °C in an Ar/H_2 stream atmosphere (volume ratio 90:10). Under an oxidizing atmosphere, the material was heated to 600 °C in a muffle furnace under air at a 5 °C min^{-1} heating rate and dwell time of 1 h. XRD and N_2 physisorption were subsequently performed to evaluate structural and morphology changes.

ζ-Potential Measurements. The ζ-potential of the sample was measured using an ELSZ-2000ZS (Otsuka Electronics) measurement system to determine the surface charges of the mesoporous LSTF oxides. Suspensions were prepared by adding 0.5 g of LSTF-00 and LSTF-40 per liter of distilled water. An ammonia solution (NH_3, 28–30 wt %, Junsei Chemical) was added to modulate the pH value to approximately 10.

RESULTS AND DISCUSSION

Material Characterization. The textural properties of LSTF solid solutions with varying SiO_2 template amounts were assessed by nitrogen physisorption analyses. The obtained curves, shown in Figure 1a, are characterized as type IV(a) isotherms.[54] From the shape of the hysteresis loop, a rough estimate of the pore morphology can be obtained. All of the synthesized materials show type H2 hysteresis, appropriate for complex pore structures in which the network effects play a major role.[42,54] The steep increase in the adsorbed volume near the saturation pressure can be attributed to the interparticle porosity, which becomes more significant with an increase in the template load. The surface area and pore volume of the perovskite increase gradually with an increase in the template load from 10 (LSTF-10) to 40 vol % (LSTF-40) (Table 1 and Figure 1a). The maximum surface area and pore volume values were determined to be 201 $m^2 g^{-1}$ and 0.411 $cm^3 g^{-1}$, respectively, for LSTF-40. Considering our previous results,[42] this represents the upper limit of surface area and porosity that can be obtained with this synthesis approach. All samples possess mesopores up to 20 nm with a broad pore size distribution. As the amount of the sacrificial template increases,

https://dx.doi.org/10.1021/acsanm.0c02456
ACS Appl. Nano Mater. 2020, 3, 11352–11362

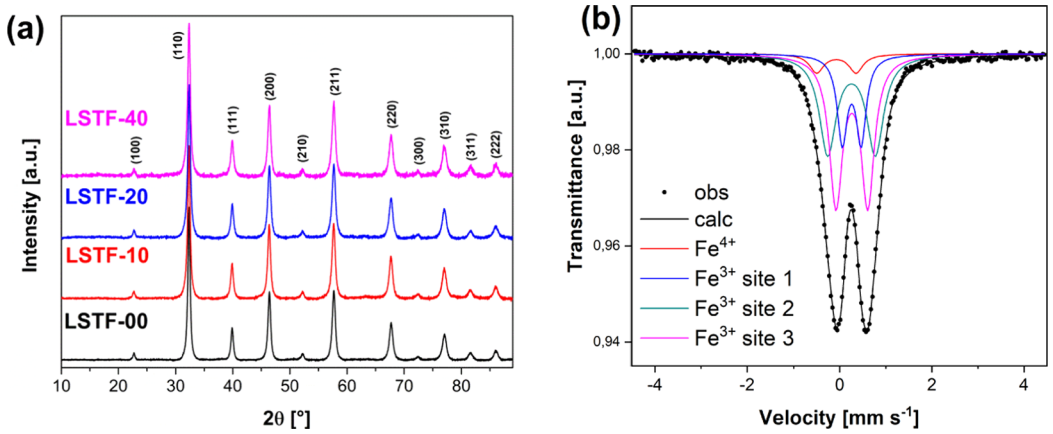

Figure 3. (a) X-ray diffractograms of the investigated LSTF samples. Data for LSTF-00 were retrieved from a previous study.[43] (b) Mössbauer spectrum of LSTF-40 was chosen as a representative system.

a progressive narrowing of the pore width is observed along with the generation of smaller mesopores down to 4 nm as the average pore width shifts toward ∼8 nm (Figure 1b). This narrowing can be ascribed to the confinement of the LSTF matrix by interpenetrating SiO_2 networks. In Figures 2 and S3, transmission electron microscopy investigations confirm for all samples a disordered distribution of pores of approximately 10 nm over polycrystalline particle aggregates several micrometers in size.

The removal of siliceous species from the matrix and the homogeneity of the LSTF elemental composition were investigated via IR and EDX spectroscopy, respectively. The effectiveness of the template-removal process for perovskite oxides prepared by a coassembly route was thoroughly investigated in our previous work.[42] It was determined that a silica template can be completely removed from the system by sodium hydroxide etching, whereas a minor portion of the initial siliceous species is incorporated into the perovskite lattice in the silicate form and cannot be eliminated. Infrared spectroscopy findings in this work indicate the same trend for Si (Figure S4). Traces of Si and much smaller amounts of Na, as residuals of the NaOH etching procedure, were also observed by X-ray photoelectron spectroscopy (XPS) (Figure S5) analyses. EDX (Figure S6) studies revealed highly homogeneous distributions of the elements and the absence of phase segregation, indicating a pure-phase solid solution for all investigated systems (Figure 2). Notwithstanding the effective template elimination, LSTF samples after the etching step showed deviations of the surface composition from nominal $La_{0.3}Sr_{0.7}Ti_{0.5}Fe_{0.5}O_{3-\delta}$ stoichiometry. Fe, Sr, and slight La deficiencies were observed for each sample, becoming more significant at increased template loadings (Table 1). These deviations, confirmed also by XPS, may arise from the formation of Fe and Sr silicates in the SiO_2-LSTF nanocomposite, as already indicated in earlier works.[42,55] The XRD analyses results in Figure 3a also show that the long-range order is retained for all nanoporous LSTF materials. Each sample displays a highly crystalline, pure cubic perovskite phase with space group *Pm*-3*m*. The average crystallite sizes decrease slightly with an increase in the template load from 22 to 18 nm, most likely due to the limited mass diffusion when the concentration of SiO_2 increases.

The Mössbauer spectra of the templated LSTF solid solutions all demonstrate similar characteristics typical of iron nuclei in a paramagnetic regime, showing the best fit with a four-component model comprised of one Fe^{4+} and three Fe^{3+} sites (Figure 3b and Table S1). Among the three ferric sites, sites 1 and 2 are assigned to octahedral Fe^{3+} cations with differing symmetrical environments due to the double substitution on the A-site of the perovskite with La and Sr species, in accordance with our previous work describing the structure of template-free prepared LSTF solid solutions (Figure S7).[43,56,57] The third ferric site, on the other hand, can be assigned to octahedral Fe^{3+} within a modified symmetrical environment associated with the interaction with the silicates in the structure[55,58,59] or to nanoscopic iron oxide in the superparamagnetic regime.[60] This second hypothesis cannot be completely neglected considering the likely chemical transformations determined by the high-temperature etching procedure during the material synthesis. The relative concentration of Fe^{3+} cations in this symmetrical environment increases with an increase in the template load from 16 to 38% at the expense of Fe^{3+}—site 1 (Table 1). The concentrations of Fe^{4+} sites in templated samples were slightly lower in comparison to that of the template-free LSTF-00 but remained relatively unaffected by variations in the template loads (Table 1).

The structural and morphological stability of highly porous LSTF-40 was investigated by exposing the perovskite to oxidizing and reducing atmospheres at 600 °C for 1 h. XRD analyses subsequent to the treatment indicate no change in the phase or microstructure. The porosity of the material was also determined to be largely unaffected, except for a minor (∼15%) loss of the surface area for LSTF-40 treated under the reducing atmosphere (Figure S8 and Table S2). The remarkable thermal stability of the highly porous LSTF points to the material's potential for high-temperature applications such as oxidation catalysis.

Catalytic Properties of Supported Pt Nanoparticles on Mesoporous LSTF. The redox-active perovskite materials along with their very large specific surface areas likely lead to a high concentration of ionic defects on the surface, which can create ideal sites for the binding of Pt NPs as well as the adsorption of reactant species.[11,14,21,61,62] Therefore, in this study, the synthesized mesoporous LSTF was used as an active support for Pt NPs. Pt particles (0.8 wt %) surrounded by cationic surfactants were uniformly dispersed by electrostatic attraction on the negatively charged LSTF-40 surface in an aqueous solution. As-prepared catalysts were dried at 350 °C and then used for CO and CH_4 oxidation tests. These

https://dx.doi.org/10.1021/acsanm.0c02456
ACS Appl. Nano Mater. 2020, 3, 11352−11362

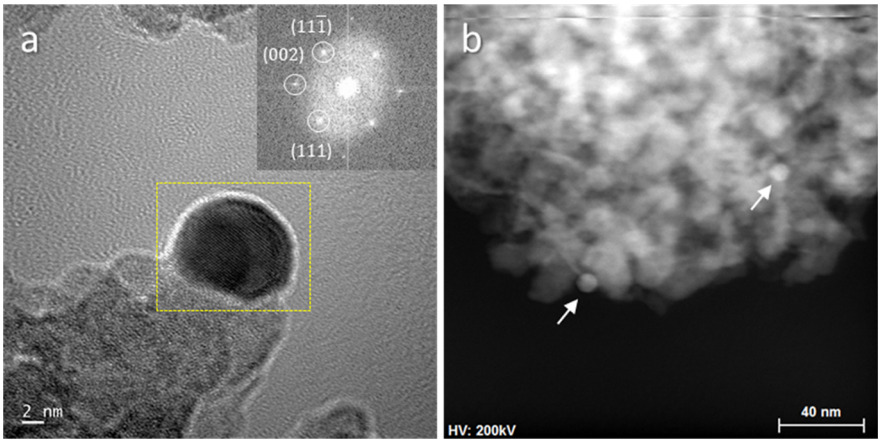

Figure 4. (a) High-resolution TEM (HR-TEM) image of Pt NP supported on the LSTF-40 oxide. The inset in (a) is the corresponding fast Fourier transform (FFT) pattern of the yellow-boxed area. (b) Representative STEM image of the Pt/LSTF-40 catalyst.

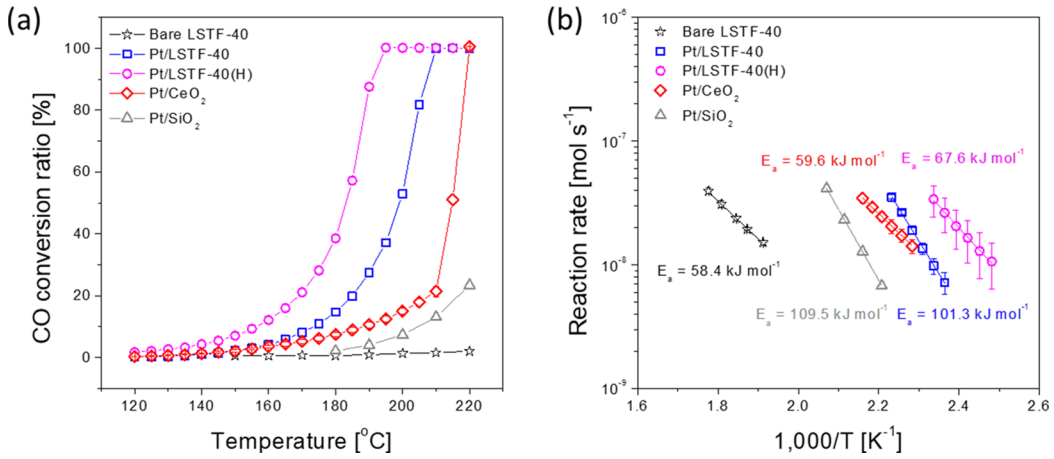

Figure 5. (a) Steady-state conversions and (b) Arrhenius plots of the CO oxidation over the investigated samples.

reactions serve as basic units in various industrial processes, such as automotive emission control and the catalytic reforming of hydrocarbons, representing low- and high-temperature reactions, respectively. Thus, they represent a suitable choice for assessing the applicability of the redox-active LSTF support with excellent oxygen supply/exchange capabilities. Electron microscopy and EDX mapping results show that Pt NPs with a size of approximately 8 nm are uniformly dispersed on LSTF oxide powders (Figures 4 and S9). In addition, EDX findings confirm that the elements of the perovskite support are still evenly distributed after Pt NP loading (Figure S10). For the detailed analysis of the Pt NP, we used the fast Fourier transform (FFT) pattern to investigate the lattice spacing of the particle, as shown in Figures 4a and S11. The FFT pattern of the yellow-boxed area of Figure 4a is shown in Figure S11 along with the inverse FFT pattern and intensity profile. We found that the average lattice spacings of {111} and {200} are 0.23 and 0.20 nm, respectively, values that are in agreement with previously reported values for Pt.[15,63] The decent dispersion of Pt is due to the nonstoichiometric surface composition of the mesoporous LSTF (Table 1). This is supported by additional ζ-potential measurements, showing that the surface charge of LSTF-40 (−30.52 mV) is lower than that (−23.98 mV) of LSTF-00. It is also noted that the Pt particles grow into larger crystallites with an average size of approximately 19 nm after a preannealing process at 350 °C for 5 h (Figure S12).

Regarding the oxidation reaction of carbon monoxide, supported Pt catalysts on LSTF-40 exhibited a T_{50} value as low as 199 °C and fully completed CO conversion at 210 °C (Figure 5a). The apparent activation energy (E_a) value, calculated from Arrhenius-type plots, was 101.3 kJ mol^{-1} for Pt/LSTF-40 (Figure 5b). Interestingly, we found that the overall rate of the reaction for Pt/LSTF-40 was faster than the sum of the rates over Pt (Pt/SiO_2) and LSTF-40 individually, even outperforming the Pt/CeO_2 catalyst (Figure 5a,b). Examining the kinetics data, the E_a value of Pt/LSTF-40 decreased from that (109.5 kJ mol^{-1}) of Pt/SiO_2. In addition, the reaction order values for Pt/LSTF-40 were −0.44 and +0.73 for CO and O_2, respectively, which differed from the expected orders (−1 and +1 for CO and O_2, respectively) on the Pt surface. The tendency to be less negative for CO and less positive for O_2 suggests that the LSTF-40 oxide alleviates the CO poisoning effect by providing spatially separated sites for oxygen supply at the Pt/LSTF-40 interface. This behavior is similar to what has been reported for CO oxidation over Pt/CeO_2, where the $Pt-CeO_2$ interface dominates the reaction under certain conditions.[64] The promotional effect at the Pt/LSTF interface is further supported by the fact that the estimated Pt dispersion value (14.5%) based on the specific rate for CO oxidation over the Pt catalyst was higher than the

https://dx.doi.org/10.1021/acsanm.0c02456
ACS Appl. Nano Mater. 2020, 3, 11352−11362

Table 2. Activity Parameters of the Investigated Catalysts[a]

sample	$E_a^{CO\ ox}$ [kJ mol^{-1}]	$m^{CO\ ox}$	$n^{CO\ ox}$	$T_{100}^{CO\ ox}$ [°C]	$E_a^{CH_4\ ox}$ [kJ mol^{-1}]	$q^{CH_4\ ox}$	$r^{CH_4\ ox}$	$T_{100}^{CH_4\ ox}$ [°C]
LSTF-40	58.4	0.98	0		120.3	0.67	0.26	
Pt/LSTF-40	101.3	−0.44	0.73	210	109.8	0.64	0	590
Pt/LSTF-40 (H)	67.6	−0.23	0.72	195	91.6	0.70	0	570
Pt/CeO_2	59.6	0	0	220	113.5			
Pt/SiO_2	109.5			250	109.8			

[a] $E_a^{CO\ ox}$, $E_a^{CH_4 ox}$, activation energies for the CO and CH_4 oxidation reactions over LSTF catalysts obtained below a conversion rate of 10%; m, n, empirically calculated reaction orders m with respect to CO and n with respect to O_2 obtained below a conversion rate of 10% (reaction rate = $kP_{CO}^{m}P_{O_2}^{n}$) for CO oxidation; and q, r, reaction orders q with respect to CH_4 and r with respect to O_2 obtained below a conversion rate of 10% (reaction rate = $kP_{CH_4}^{q}P_{O_2}^{r}$) for CH_4 oxidation. The parameters for the template-free material (LSTF-00) were taken from the literature,[43] and the reaction orders for Pt/CeO_2 were taken from the literature.[13]

measured dispersion value (2.5%) in Pt/LSTF (Table S3). Several previous studies also reported that interplay between metal NPs and perovskite oxides can accelerate the CO oxidation rate.[65,66]

Next, we investigated the stability of the catalyst and observed how the catalytic properties changed with a thermal treatment by calcination of the Pt/LSTF-40 catalyst at 550 °C for 48 h in an air atmosphere. It was noted that because LSTF was synthesized at 600 °C, we examined a postannealing effect below the synthesis temperature to exclude the influence of the structural transformation of the oxide support. The heat-treated catalyst is referred to here as Pt/LSTF-40 (H). Interestingly, light-off initiated at the lower temperature after thermal treatment, as shown in Figure 5a. This enhanced activity leads to complete CO conversion of Pt/LSTF-40 (H) at 195 °C with a T_{50} value of 183 °C, which is approximately 15 °C lower than that of Pt/LSTF (Figure 5a). The E_a value was 67.6 kJ mol^{-1} for Pt/LSTF-40 (H) (Figure 5b). Consequently, the thermal treatment improved the CO oxidation activity by approximately 3.7 times with respect to the Pt/LSTF-40 catalyst at the same reaction temperature (150 °C), as shown in Figure S13a. This phenomenon reflects the enhanced synergistic interaction between the metal and the support, as evidenced by the following observations. First, the E_a value (67.6 kJ mol^{-1}) of Pt/LSTF-40 (H) shows more of a decrease from that of Pt/SiO_2 (109.5 kJ mol^{-1}). Second, the reaction order for CO was −0.23, which is closer to zero and which deviates more from the characteristic on the Pt surface (Table 2). Finally, we observed a further increment of the estimated dispersion value (51.1%) after postannealing treatment (Table S3), which strongly indicates an enhanced promotional effect at the Pt/LSTF interface. It should be noted that there was no considerable change in the size of the Pt NPs before or after heat treatment (Figure S12).

To provide further evidence of the improved metal−support interaction, H_2-TPR experiments were conducted, as shown in Figure 6. We found that the intensity of the first peak present below 150 °C increased significantly after heat treatment. This peak can be interpreted as the reduction of PtO species,[67−69] but the PtO reduction does not appear to contribute significantly to the peak evolution as the catalyst showed similar metal dispersions before and after heat treatment. Instead, the evolution of the peak is likely due to the reduction of LSTF adjacent to Pt, where hydrogen can easily spill over onto the oxide surface, suggesting that heat treatment prompted the promotional effect at the Pt/LSTF interface.[67−69] The second peak at 186 °C is attributed to the reduction of Fe^{4+} to the Fe^{3+} species, and it disappears after heat treatment. The presence of Fe^{4+} species in the LSTF-40

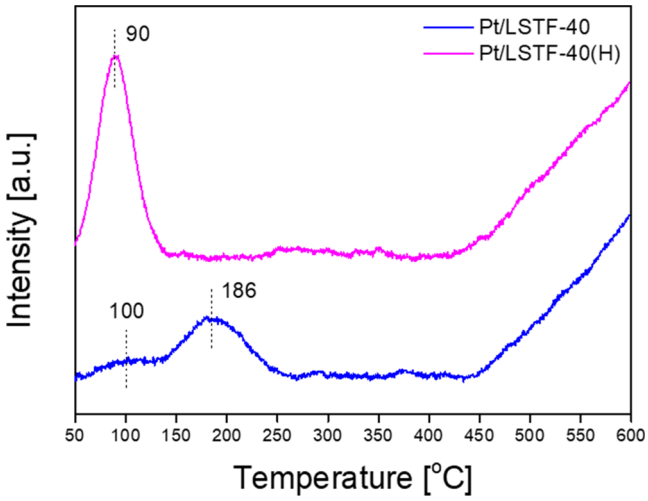

Figure 6. H_2-TPR profiles of the Pt/LSTF-40 and Pt/LSTF-40(H) catalysts.

oxide confirms the result of Mössbauer spectroscopy that Fe^{4+} sites exist with Fe^{3+} sites. Further reduction of Fe^{3+} to Fe^{2+} started from approximately 450 °C.

The CH_4 oxidation reaction, another catalytic test, was conducted to evaluate the activity of the Pt/LSTF sample (Figure 7a,b). The reaction products were exclusively CO_2 and H_2O in all tests, indicating complete oxidation. In the light-off curves, Pt/LSTF-40 achieved 50% methane conversion at 498 °C (Figure 7a). From the Arrhenius-type plots, the E_a value was found to be 109.8 kJ mol^{-1} (Figure 7b). Akin to the CO oxidation results, the measured reaction rate for Pt/LSTF-40 was larger than the sum of the individual rates for Pt (Pt/SiO_2) and LSTF-40; therefore, the improved catalytic activity can be ascribed to the interactive effect between the oxide and the metal. We did not observe a noticeable difference in the E_a values between the Pt/LSTF-40 and Pt/SiO_2 catalysts (Figure 7b). However, the reaction orders for CH_4 and O_2 were 0.64 and 0 (Table 2), respectively, which deviated from the expected orders (+1 and −0.5 for CH_4 and O_2, respectively) on the Pt surface at a methane-to-oxygen ratio of 0.25.[70,71] Thus, we can conclude that CH_4 oxidation is not limited to solely the Pt surface but also occurs at the Pt/LSTF interface.

Like CO oxidation, a postannealing treatment improves the reaction rate in CH_4 oxidation. After thermal treatment at 550 °C for 48 h in air, the CH_4 oxidation rate improved by approximately 1.9 times with respect to an unaged catalyst sample (Figure S13b). Thus, although there were differences in the degree of improvement, heat treatment promotes oxidation

https://dx.doi.org/10.1021/acsanm.0c02456
ACS Appl. Nano Mater. 2020, 3, 11352−11362

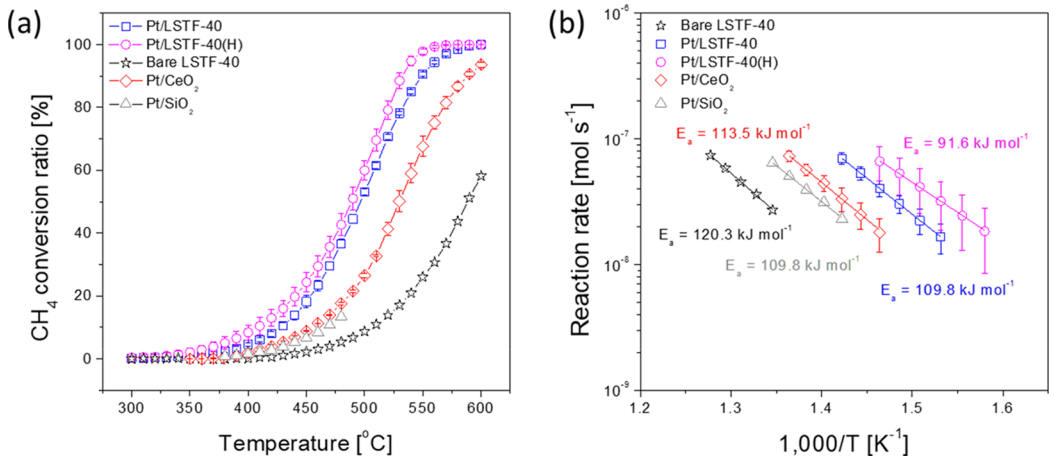

Figure 7. (a) Steady-state conversions and (b) Arrhenius plots for the CH_4 oxidation reaction over the investigated samples.

for both CO and CH_4, which is a reflection of the activation of the Pt/LSTF interface. However, another explanation is also possible: an increased segregation level of Sr and the associated formation of highly oxidative oxygen (O_2^{2-}/O^-) species on the oxide surface (Tables 3 and S4 and Figure S14). As found in

Table 3. X-ray Photoelectron Spectroscopy (XPS) Results

sample	La/Sr atomic ratio	Fe/Ti atomic ratio	lattice O [%]	O_2^{2-}/O^- [%]
Pt/LSTF-40	0.58	0.46	72.4	3.6
Pt/LSTF-40 (H)	0.43	0.46	72.0	7.7

our previous studies[72,73] as well as in several other works,[74−76] unless a thick and dense layer is formed on the oxide surface, Sr-enriched surface phases can facilitate the catalytic oxidation of methane. It has been demonstrated that the basicity of Sr-enriched $SrTiO_3$ oxides plays a fundamental role in the dehydrogenation and dehydration of several organic compounds, including methane.[75] Moreover, highly oxidative oxygen (O_2^{2-}/O^-) species present in A-site-deficient perovskites as a result of surface oxygen vacancies can improve the catalytic activity of methane.[72,73] Considering these results as a whole, we can conclude that chemically complex high-surface perovskite oxides are promising active support materials that can promote the reactivity of Pt nanocatalysts.

Catalytic Properties of Bare Mesoporous LSTF. In addition to evaluating the properties of mesoporous LSTF materials as noble-metal catalyst supports, the assessment of the catalytic performance of the bare LSTF materials covers an important aspect in light of the development of sustainable catalysis systems. Related to this purpose, we evaluated the catalytic properties of mesoporous perovskites as a function of the specific surface area with respect to the total methane oxidation reaction. The light-off curves depicted in Figure 8 show that the catalytic efficiency decreases with the materials' porosity. This counterintuitive result has two major explanations. First, as shown by the EDX analysis (Table 1), the higher the specific surface area of the materials, the lower the amount of iron found. Fe species have been identified as active sites for methane oxidation over LSTF solid solutions,[43] and their decreased concentration is likely correlated with the occurrence of competitive reactions with the later-removed siliceous phase, as corroborated by Mössbauer spectroscopy findings. A second reason for the catalytic activity loss is

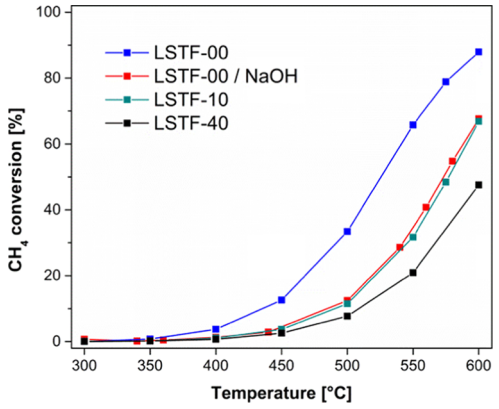

Figure 8. Steady-state conversions obtained for CH_4 oxidation over the investigated LSTF samples to provide evidence of the effect of the surface modification on the catalytic performance.

NaOH treatment for removal of the template. As shown in Figure 8, NaOH treatment deteriorates the oxidative reactivity of the template-free LSTF. For example, the methane conversion rates measured before and after NaOH etching at 600 °C are 88 and 68%, respectively, confirming that the etching process reduces the catalytic performance by approximately 20%. This performance decrease could be likely related to the formation of a Na-containing oxide passivation layer (see Figure S5e) that inhibits the release of β-oxygen species. These findings conclusively highlight the influence of the template-removal step on the surface properties and the complexity of designing highly porous perovskite oxides for high-temperature catalysis applications.

CONCLUSIONS

In the present work, we successfully prepared highly nanoporous LSTF solid solutions and evaluated their properties as support materials for noble-metal catalysts in oxidation reactions. Using a SiO_2 endotemplating route, substantial surface areas and pore volumes of up to 201 $m^2\ g^{-1}$ and 0.411 $cm^3\ g^{-1}$, respectively, could be obtained by varying the template loading from 10 to 40 vol %. The high structural stability of the materials with the highest porosity (LSTF-40) in both oxidizing and reducing high-temperature conditions made them suitable for use as a metal catalyst support. When Pt NPs (0.8 wt %) were dispersed, the mesoporous LSTF-40

https://dx.doi.org/10.1021/acsanm.0c02456
ACS Appl. Nano Mater. 2020, 3, 11352−11362

exhibited improved activity for the CO and CH_4 oxidation reactions compared to commercially available SiO_2 and CeO_2 supports due to the promotional effect at the Pt/LSTF-40 interface. After an additional thermal treatment at 550 °C for 48 h, the reaction rates were further improved, an outcome likely related to the enhanced synergistic interaction between the metal and the support as well as to the higher surface Sr segregation and the higher concentration of oxygen defects, as revealed by XPS studies. Such chemical modification of the surface species is a feature typical of only perovskite structures. Therefore, it was not surprising that benchmark tests using Pt nanoparticles supported on CeO_2 or SiO_2 showed lower performance than on our nanoscaled materials for both oxidation reactions. Despite the attractive perspective when using mesoporous perovskites as standalone catalysts, the design of such systems is highly challenging. Methane oxidation tests indicated how the template-removal step affects the material surface chemistry and therefore the catalytic response. It is well known that the catalytic performance capabilities of supported noble-metal catalysts depend on various parameters, such as the shape and size of the metal nanoparticles, the surface composition and morphology of the support material, the nature and concentration of the reactants, the density of active site pairs, and the catalyst pretreatment.[4,7,14,77−79] The attractive morphological properties and chemical activity of highly nanoporous LSTF point to the strong application potential of this nanostructured material with further optimization of these parameters.

■ ASSOCIATED CONTENT

Supporting Information

The Supporting Information is available free of charge at https://pubs.acs.org/doi/10.1021/acsanm.0c02456.

XPS spectra, detailed TEM analysis of nanoporous oxides and nanoparticle distribution, Mössbauer spectra and parameters, and description of the catalytic reactor (PDF)

■ AUTHOR INFORMATION

Corresponding Authors

WooChul Jung − *Department of Materials Science and Engineering, Korea Advanced Institute of Science and Technology, Daejeon 34141, Republic of Korea*; Email: wcjung@kaist.ac.kr

Simone Mascotto − *Institut für Anorganische und Angewandte Chemie, Universität Hamburg, D-20146 Hamburg, Germany*; orcid.org/0000-0002-3503-6391; Email: simone.mascotto@chemie.uni-hamburg.de

Authors

Buğra Kayaalp − *Institut für Anorganische und Angewandte Chemie, Universität Hamburg, D-20146 Hamburg, Germany*

Siwon Lee − *Department of Materials Science and Engineering, Korea Advanced Institute of Science and Technology, Daejeon 34141, Republic of Korea*

Luca Nodari − *Istituto di Chimica della Materia Condensata e di Tecnologie per l'Energia, ICMATE-CNR, Padova 35127, Italy; Dipartimento di Scienze Chimiche, Università di Padova, Padova 35131, Italy*

Jongsu Seo − *Department of Materials Science and Engineering, Korea Advanced Institute of Science and Technology, Daejeon 34141, Republic of Korea*

Seunghyun Kim − *Department of Materials Science and Engineering, Korea Advanced Institute of Science and Technology, Daejeon 34141, Republic of Korea*

Complete contact information is available at: https://pubs.acs.org/10.1021/acsanm.0c02456

Author Contributions

⊥B.K. and S.L. contributed equally.

Notes

The authors declare no competing financial interest.

■ ACKNOWLEDGMENTS

Uta Sazama, Sandra König, Isabelle Nevoigt, and Andreas Kornowski are kindly acknowledged for the support given with regard to the material characterization. The authors thank Prof. Michael Fröba of the University of Hamburg for inspiring discussions. S.L., J.S., S.K., and W.J. were financially supported by the Korea Institute of Energy Technology Evaluation and Planning (KETEP) and the Ministry of Trade, Industry & Energy (MOTIE) of the Republic of Korea (Nos. 20173020032120 and 20194030202360).

■ REFERENCES

(1) Chen, J.; Arandiyan, H.; Gao, X.; Li, J. Recent Advances in Catalysts for Methane Combustion. *Catal. Surv. Asia* **2015**, *19*, 140−171.

(2) Cargnello, M.; Gorte, P.; Fornasiero, J. R. Opportunities for Tailoring Catalytic Properties Through Metal-Support Interactions. *Catal. Lett.* **2012**, *142*, 1043−1048.

(3) Bera, P.; Patil, K. C.; Jayaram, V.; Subbanna, G. N.; Hegde, M. S. Ionic Dispersion of Pt and Pd on CeO_2 by Combustion Method: Effect of Metal-Ceria Interaction on Catalytic Activities for NO Reduction and CO and Hydrocarbon Oxidation. *J. Catal.* **2000**, *196*, 293−301.

(4) Miller, J. B.; Malatpure, M. Pd Catalysts for Total Oxidation of Methane: Support Effects. *Appl. Catal., A* **2015**, *495*, 54−62.

(5) An, K.; Alayoglu, S.; Musselwhite, N.; Plamthottam, S.; Lindeman, A. E.; Somorjai, G. A.; Melaet, G. Enhanced CO Oxidation Rates at the Interface of Mesoporous Oxides and Pt Nanoparticles. *J. Am. Chem. Soc.* **2013**, *135*, 16689−16696.

(6) Conner, W. C.; Falconer, J. L. Spillover in Heterogeneous Catalysis. *Chem. Rev.* **1995**, *95*, 759−788.

(7) Bozo, C.; Guilhaume, N.; Herrmann, J. M. Role of the Ceria-Zirconia Support in the Reactivity of Platinum and Palladium Catalysts for Methane Total Oxidation under Lean Conditions. *J. Catal.* **2001**, *203*, 393−406.

(8) Gatla, S.; Aubert, D.; Agostini, G.; Mathon, O.; Pascarelli, S.; Lunkenbein, T.; Willinger, M. G.; Kaper, H. Room-Temperature CO Oxidation Catalyst: Low-Temperature Metal−Support Interaction between Platinum Nanoparticles and Nanosized Ceria. *ACS Catal.* **2016**, *6*, 6151−6155.

(9) Avila, M. S.; Vignatti, C. I.; Apesteguía, C. R.; Garetto, T. F. Effect of Support on the Deep Oxidation of Propane and Propylene on Pt-Based Catalysts. *Chem. Eng. J.* **2014**, *241*, 52−59.

(10) Groppi, G.; Cristiani, C.; Lietti, L.; Ramella, C.; Valentini, M.; Forzatti, P. Effect of Ceria on Palladium Supported Catalysts for High Temperature Combustion of CH_4 under Lean Conditions. *Catal. Today* **1999**, *50*, 399−412.

(11) Nartova, A. V.; Kovtunova, L. M.; Khudorozhkov, A. K.; Shefer, K. I.; Shterk, G. V.; Kvon, R. I.; Bukhtiyarov, V. I. Influence of Preparation Conditions on Catalytic Activity and Stability of Platinum on Alumina Catalysts in Methane Oxidation. *Appl. Catal., A* **2018**, *566*, 174−180.

(12) Schwartz, W. R.; Pfefferle, L. D. Combustion of Methane over Palladium-Based Catalysts: Support Interactions. *J. Phys. Chem. C* **2012**, *116*, 8571−8578.

(13) Cargnello, M.; Doan-Nguyen, V. V. T.; Gordon, T. R.; Diaz, R. E.; Stach, E. A.; Gorte, R. J.; Fornasiero, P.; Murray, C. B. Control of Metal Nanocrystal Size Reveals Metal-Support Interface Role for Ceria Catalysts. *Science* **2013**, *341*, 771−774.
(14) Pakharukova, V. P.; Pakharukov, I. Y.; Bukhtiyarov, V. I.; Parmon, V. N. Alumina-Supported Platinum Catalysts: Local Atomic Structure and Catalytic Activity for Complete Methane Oxidation. *Appl. Catal., A* **2014**, *486*, 12−18.
(15) Lee, S.; Seo, J.; Jung, W. Sintering-Resistant Pt@CeO_2 Nanoparticles for High-Temperature Oxidation Catalysis. *Nanoscale* **2016**, *8*, 10219−10228.
(16) Prieto, G.; Zecevic, J.; Friedrich, H.; de Jong, K. P.; de Jongh, P. E. Towards Stable Catalysts by Controlling Collective Properties of Supported Metal Nanoparticles. *Nat. Mater.* **2013**, *12*, 34−39.
(17) Farmer, J. A.; Campbell, C. T. Ceria Maintains Smaller Metal Catalyst Particles by Strong Metal-Support Bonding. *Science* **2010**, *329*, 933−937.
(18) Parinyaswan, A.; Pongstabodee, S.; Luengnaruemitchai, A. Catalytic Performances of Pt-Pd/CeO_2 Catalysts for Selective CO Oxidation. *Int. J. Hydrogen Energy* **2006**, *31*, 1942−1949.
(19) Zhu, X.; Li, K.; Neal, L. M.; Li, F. Perovskites as Geo-Inspired Oxygen Storage Materials for Chemical Looping and Three-Way Catalysis - A Perspective. *ACS Catal.* **2018**, *8*, 8213−8236.
(20) Scholz, J.; Garbujo, A.; Kayaalp, B.; Klauke, K.; Glisenti, A.; Mascotto, S. Functional Nanostructured Perovskite Oxides from Radical Polymer Precursors. *Inorg. Chem.* **2019**, *58*, 15942−15952.
(21) Ligthart, D. A. J. M.; van Santen, R. A.; Hensen, E. J. M. Supported Rhodium Oxide Nanoparticles as Highly Active CO Oxidation Catalysts. *Angew. Chem., Int. Ed.* **2011**, *50*, 5306−5310.
(22) Bisht, A.; Sihag, A.; Satyaprasad, A.; Mallajosyala, S. S.; Sharma, S. Pt Metal Supported and Pt^{4+}Doped $La_{1-x}Sr_xCoO_3$: Non-Performance of Pt^{4+} and Reactivity Differences with Pt Metal. *Catal. Lett.* **2018**, *148*, 1965−1977.
(23) Zhou, K.; Chen, H.; Tian, Q.; Hao, Z.; Shen, D.; Xu, X. Pd-Containing Perovskite-Type Oxides Used for Three-Way Catalysts. *J. Mol. Catal., A* **2002**, *189*, 225−232.
(24) Ji, K.; Dai, H.; Deng, J.; Zhang, L.; Wang, F.; Jiang, H.; Au, C. T. Three-Dimensionally Ordered Macroporous $SrFeO_{3-\delta}$ with High Surface Area: Active Catalysts for the Complete Oxidation of Toluene. *Appl. Catal., A* **2012**, *425−426*, 153−160.
(25) Alifanti, M.; Kirchnerova, J.; Delmon, B.; Klvana, D. Methane and Propane Combustion over Lanthanum Transition-Metal Perovskites: Role of Oxygen Mobility. *Appl. Catal., A* **2004**, *262*, 167−176.
(26) Wei, X.; Hug, P.; Figi, R.; Trottmann, M.; Weidenkaff, A.; Ferri, D. Catalytic Combustion of Methane on Nano-Structured Perovskite-Type Oxides Fabricated by Ultrasonic Spray Combustion. *Appl. Catal., B* **2010**, *94*, 27−37.
(27) Arandiyan, H.; Dai, H.; Deng, J.; Wang, Y.; Sun, H.; Xie, S.; Bai, B.; Liu, Y.; Ji, K.; Li, J. Three-Dimensionally Ordered Macroporous La0.6Sr0.4MnO3 Supported Ag Nanoparticles for the Combustion of Methane. *J. Phys. Chem. C* **2014**, *118*, 14913−14928.
(28) Liu, Y.; Dai, H.; Deng, J.; Xie, S.; Yang, H.; Tan, W.; Han, W.; Jiang, Y.; Guo, G. Mesoporous Co_3O_4-Supported Gold Nanocatalysts: Highly Active for the Oxidation of Carbon Monoxide, Benzene, Toluene, and o-Xylene. *J. Catal.* **2014**, *309*, 408−418.
(29) Mao, M.; Lv, H.; Li, Y.; Yang, Y.; Zeng, M.; Li, N.; Zhao, X. Metal Support Interaction in Pt Nanoparticles Partially Confined in the Mesopores of Microsized Mesoporous CeO_2 for Highly Efficient Purification of Volatile Organic Compounds. *ACS Catal.* **2016**, *6*, 418−427.
(30) Park, J. E.; Kim, K. B.; Seo, K. W.; Song, K. S.; Park, E. D. Propane Combustion over Supported Pt Catalysts. *Res. Chem. Intermed.* **2011**, *37*, 1135−1143.
(31) Ramirez, A. A.; Benard, S.; Anne, G.-F.; Jones, J. P.; Heitz, M. Treatment of Air Polluted with Methanol Vapours in Biofilters with and without Percolation. *Can. J. Civ. Eng.* **2009**, *36*, 1911−1918.
(32) Liu, Y.; Dai, H.; Du, Y.; Deng, J.; Zhang, L.; Zhao, Z.; Tong, C. Controlled Preparation and High Catalytic Performance of Three-Dimensionally Ordered Macroporous $LaMnO_3$ with Nanovoid Skeletons for the Combustion of Toluene. *J. Catal.* **2012**, *287*, 149−160.
(33) Haneda, M.; Sasaki, M.; Hamada, H.; Ozawa, M. Effect of Pt Dispersion on the Catalytic Activity of Supported Pt Catalysts for Diesel Hydrocarbon Oxidation. *Top. Catal.* **2013**, *56*, 249−254.
(34) Joo, S. H.; Choi, S. J.; Oh, I.; Kwak, J.; Liu, Z.; Terasaki, O.; Ryoo, R. Ordered Nanoporous Arrays of Carbon Supporting High Dispersions of Platinum Nanoparticles. *Nature* **2001**, *412*, 169−172.
(35) Taguchi, A.; Schüth, F. Ordered Mesoporous Materials in Catalysis. *Microporous Mesoporous Mater.* **2005**, *77*, 1−45.
(36) Gommes, C. J.; Prieto, G.; Zecevic, J.; Vanhalle, M.; Goderis, B.; de Jong, K. P.; de Jongh, P. E. Mesoscale Characterization of Nanoparticles Distribution Using X-Ray Scattering. *Angew. Chem., Int. Ed.* **2015**, *54*, 11804−11808.
(37) de Jongh, P. E.; Eggenhuisen, T. M. Melt Infiltration: An Emerging Technique for the Preparation of Novel Functional Nanostructured Materials. *Adv. Mater.* **2013**, *25*, 6672−6690.
(38) Prieto, G.; Shakeri, M.; de Jong, K. P.; de Jongh, P. E. Quantitative Relationship between Support Porosity and the Stability of Pore-Confined Metal Nanoparticles Studied on CuZnO/SiO_2 Methanol Synthesis Catalysts. *ACS Nano* **2014**, *8*, 2522−2531.
(39) Prieto, G.; Meeldijk, J. D.; de Jong, K. P.; de Jongh, P. E. Interplay between Pore Size and Nanoparticle Spatial Distribution: Consequences for the Stability of CuZn/SiO_2 Methanol Synthesis Catalysts. *J. Catal.* **2013**, *303*, 31−40.
(40) Sarshar, Z.; Kleitz, F.; Kaliaguine, S. Novel Oxygen Carriers for Chemical Looping Combustion: $La_{1-x}Ce_xBO_3$ (B = Co, Mn) Perovskites Synthesized by Reactive Grinding and Nanocasting. *Energy Environ. Sci.* **2011**, *4*, 4258.
(41) Nair, M. M.; Kleitz, F.; Kaliaguine, S. Kinetics of Methanol Oxidation over Mesoporous Perovskite Catalysts. *ChemCatChem* **2012**, *4*, 387−394.
(42) Kayaalp, B. E.; Lee, Y. J.; Kornowski, A.; Gross, S.; D'Arienzo, M.; Mascotto, S. Cooperative Assembly Synthesis of Mesoporous $SrTiO_3$ with Enhanced Photocatalytic Properties. *RSC Adv.* **2016**, *6*, 90401−90409.
(43) Kayaalp, B.; Lee, S.; Klauke, K.; Jongsu, S.; Nodari, L.; Kornowski, A.; Jung, W.; Mascotto, S. Template-Free Mesoporous $La_{0.3}Sr_{0.7}Fe_xTi_{1-X}O_{3\pm\delta}$ for CH_4 and CO Oxidation Catalysis. *Appl. Catal., B* **2019**, *245*, 536−545.
(44) Fan, X.; Wang, Y.; Chen, X.; Gao, L.; Luo, W.; Yuan, Y.; Li, Z.; Yu, T.; Zhu, J.; Zou, Z. Facile Method to Synthesize Mesoporous Multimetal Oxides ($ATiO_3$, A=Sr, Ba) with Large Specific Surface Areas and Crystalline Pore Walls. *Chem. Mater.* **2010**, *22*, 1276−1278.
(45) Wang, W.; Zhu, Y.; Zhang, S.; Deng, J.; Huang, Y.; Yan, W. Flotation Behaviors of Perovskite, Titanaugite, and Magnesium Aluminate Spinel Using Octyl Hydroxamic Acid as the Collector. *Minerals* **2017**, *7*, No. 134.
(46) Zheng, Y.; Cui, Y.; Wang, W. Activation Mechanism of Lead Ions in Perovskite Flotation with Octyl Hydroxamic Acid Collector. *Minerals* **2018**, *8*, No. 341.
(47) Luu, M. D.; Dao, N. N.; Van Nguyen, D.; Pham, N. C.; Vu, T. N.; Doan, T. D. A New Perovskite-Type $NdFeO_3$ Adsorbent: Synthesis, Characterization, and As(V) Adsorption. *Adv. Nat. Sci. Nanosci. Nanotechnol.* **2016**, *7*, No. 025015.
(48) Jiang, P.; Lu, G.; Guo, Y.; Guo, Y.; Zhang, S.; Wang, X. Preparation and Properties of a γ-Al_2O_3 Washcoat Deposited on a Ceramic Honeycomb. *Surf. Coat. Technol.* **2005**, *190*, 314−320.
(49) Gómez, D. M.; Gatica, J. M.; Hernández-Garrido, J. C.; Cifredo, G. A.; Montes, M.; Sanz, O.; Rebled, J. M.; Vidal, H. A Novel CoO_x/La-Modified-CeO_2 Formulation for Powdered and Washcoated onto Cordierite Honeycomb Catalysts with Application in VOCs Oxidation. *Appl. Catal., B* **2014**, *144*, 425−434.
(50) Joo, S. H.; Park, J. Y.; Tsung, C.-K.; Yamada, Y.; Yang, P.; Somorjai, G. A. Thermally Stable Pt/Mesoporous Silica Core−Shell Nanocatalysts for High-Temperature Reactions. *Nat. Mater.* **2009**, *8*, 126−131.
(51) Kim, S.; Lee, S.; Jung, W. Sintering Resistance of Pt@SiO_2 Core-Shell Catalyst. *ChemCatChem* **2019**, *11*, 4653−4659.

https://dx.doi.org/10.1021/acsanm.0c02456
ACS Appl. Nano Mater. 2020, 3, 11352−11362

(52) Brunauer, S.; Emmett, P. H.; Teller, E. Adsorption of Gases in Multimolecular Layers. *J. Am. Chem. Soc.* **1938**, *60*, 309−319.
(53) Ravikovitch, P. I.; Neimark, A. V. Characterization of Micro- and Mesoporosity in SBA-15 Materials from Adsorption Data by the NLDFT Method. *J. Phys. Chem. B* **2001**, *105*, 6817−6823.
(54) Thommes, M.; Kaneko, K.; Neimark, A. V.; Olivier, J. P.; Rodriguez-Reinoso, F.; Rouquerol, J.; Sing, K. S. W. Physisorption of Gases, with Special Reference to the Evaluation of Surface Area and Pore Size Distribution (IUPAC Technical Report). *Pure Appl. Chem.* **2015**, *87*, 1051−1069.
(55) Zhang, C.-H.; Wan, H.-J.; Yang, Y.; Xiang, H.-W.; Li, Y.-W. Study on the Iron−Silica Interaction of a Co-Precipitated Fe/SiO2 Fischer−Tropsch Synthesis Catalyst. *Catal. Commun.* **2006**, *7*, 733−738.
(56) Clevenger, T. R. Effect of Fe^{4+} in the System $SrFeO_3$-$SrTiO_3$. *J. Am. Ceram. Soc.* **1963**, *46*, 207−210.
(57) Leontiou, A. A.; Ladavos, A. K.; Giannakas, A. E.; Bakas, T. V.; Pomonis, P. J. A Comparative Study of Substituted Perovskite-Type Solids of Oxidic $La_{1-x}Sr_xFeO_{3\pm\delta}$ and Chlorinated $La_{1-x}Sr_xFeO_{3\pm\delta}Cl_\sigma$ Form: Catalytic Performance for CH_4 Oxidation by O. *J. Catal.* **2007**, *251*, 103−112.
(58) Coey, J. M. D. Mössbauer Spectroscopy of Silicate Minerals. In *Mössbauer Spectroscopy Applied to Inorganic Chemistry*; Springer US: Boston, MA, 1984; pp 443−509.
(59) Bhagwat, S.; Yedave, S. N.; Phase, D. M.; Chaudhari, S. M.; Kanetkar, S. M.; Ogale, S. B. Ion-Beam Mixing at the Fe/SiO_2 Interface: A Conversion-Electron Mössbauer Spectroscopy and x-Ray-Diffraction Study. *Phys. Rev. B* **1989**, *40*, No. 700.
(60) Kündig, W.; Bömmel, H.; Constabaris, G.; Lindquist, R. H. Some Properties of Supported Small A−Fe_2O_3 Particles Determined with the Mössbauer Effect. *Phys. Rev.* **1966**, *142*, No. 327.
(61) Kim, M.-Y.; Park, J.-H.; Shin, C.-H.; Han, S.-W.; Gon, S. Dispersion Improvement of Platinum Catalysts Supported on Silica, Silica-Alumina and Alumina by Titania Incorporation and pH Adjustment. *Catal. Lett.* **2009**, *133*, 288−297.
(62) Liu, M. H.; Chen, Y. W.; Lin, T. S.; Mou, C. Y. Defective Mesocrystal ZnO-Supported Gold Catalysts: Facilitating CO Oxidation via Vacancy Defects in ZnO. *ACS Catal.* **2018**, *8*, 6862−6869.
(63) Sarkar, B.; Pendem, C.; Konathala, L. N. S.; Sasaki, T.; Bal, R. Pt Nanoparticle Supported on Nanocrystalline CeO_2: Highly Selective Catalyst for Upgradation of Phenolic Derivatives Present in Bio-Oil. *J. Mater. Chem. A* **2014**, *2*, 18398−18404.
(64) Bunluesin, T.; Putna, E. S.; Gorte, R. J. A Comparison of CO Oxidation on Ceria-Supported Pt, Pd, and Rh. *Catal. Lett.* **1996**, *41*, 1−5.
(65) Neagu, D.; Papaioannou, E. I.; Ramli, W. K. W.; Miller, D. N.; Murdoch, B. J.; Ménard, H.; Umar, A.; Barlow, A. J.; Cumpson, P. J.; Irvine, J. T. S.; Metcalfe, I. S. Demonstration of Chemistry at a Point through Restructuring and Catalytic Activation at Anchored Nanoparticles. *Nat. Commun.* **2017**, *8*, No. 1855.
(66) Jo, Y. R.; Koo, B.; Seo, M. J.; Kim, J. K.; Lee, S.; Kim, K.; Han, J. W.; Jung, W. C.; Kim, B. J. Growth Kinetics of Individual Co Particles Ex-Solved on $SrTi_{0.75}Co_{0.25}O_{3-}$? Polycrystalline Perovskite Thin Films. *J. Am. Chem. Soc.* **2019**, *141*, 6690−6697.
(67) Wang, F.; Xu, Y.; Zhao, K.; He, D. Preparation of Palladium Supported on Ferric Oxide Nano-Catalysts for Carbon Monoxide Oxidation in Low Temperature. *Nano-Micro Lett.* **2014**, *6*, 233−241.
(68) Musolino, M. G.; Busacca, C.; Mauriello, F.; Pietropaolo, R. Aliphatic Carbonyl Reduction Promoted by Palladium Catalysts under Mild Conditions. *Appl. Catal., A* **2010**, *379*, 77−86.
(69) Jia, J.; Shen, J.; Lin, L.; Xu, Z.; Zhang, T.; Liang, D. A Study on Reduction Behaviors of the Supported Platinum−Iron Catalysts. *J. Mol. Catal., A* **1999**, *138*, 177−184.
(70) Lee, J. H.; Trimm, D. L. Catalytic Combustion of Methane. *Fuel Process. Technol.* **1995**, *42*, 339−359.
(71) Yao, Y.-F. Y. Oxidation of Alkanes over Noble Metal Catalysts. *Ind. Eng. Chem. Prod. Res. Dev.* **1980**, *19*, 293−298.
(72) Kayaalp, B.; Klauke, K.; Biesuz, M.; Iannaci, A.; Sglavo, V. M.; D'Arienzo, M.; Noei, H.; Lee, S.; Jung, W.; Mascotto, S. Surface Reconstruction Under the Exposure of Electric Fields Enhances the Reactivity of Donor-Doped $SrTiO_3$. *J. Phys. Chem. C* **2019**, *123*, 16883−16892.
(73) Klauke, K.; Kayaalp, B.; Biesuz, M.; Iannaci, A.; Sglavo, V. M.; D'Arienzo, M.; Lee, S.; Jongsu, S.; Jung, W.; Mascotto, S. Enhancement of the $SrTiO_3$ Surface Reactivity by Exposure to Electric Fields. *ChemNanoMat* **2019**, *5*, 948−956.
(74) Polo-Garzon, F.; Fung, V.; Liu, X.; Hood, Z. D.; Bickel, E. E.; Bai, L.; Tian, H.; Foo, G. S.; Chi, M.; Jiang, D. E.; Wu, Z. Understanding the Impact of Surface Reconstruction of Perovskite Catalysts on CH_4 Activation and Combustion. *ACS Catal.* **2018**, *8*, 10306−10315.
(75) Polo-Garzon, F.; Yang, S. Z.; Fung, V.; Foo, G. S.; Bickel, E. E.; Chisholm, M. F.; Jiang, D. E.; Wu, Z. Controlling Reaction Selectivity through the Surface Termination of Perovskite Catalysts. *Angew. Chem., Int. Ed.* **2017**, *56*, 9820−9824.
(76) Bai, L.; Polo-Garzon, F.; Bao, Z.; Luo, S.; Moskowitz, B. M.; Tian, H.; Wu, Z. Impact of Surface Composition of $SrTiO_3$ Catalysts for Oxidative Coupling of Methane. *ChemCatChem* **2019**, *11*, 2107−2117.
(77) Roth, D.; Gelin, P.; Tena, E.; Primet, M. Combustion of Methane at Low Temperature over Pd and Pt Catalysts Supported on Al_2O_3, SnO_2 and Al_2O_3-Grafted SnO_2. *Top. Catal.* **2001**, *16−17*, 77−82.
(78) Beck, I. E.; Bukhtiyarov, V. I.; Pakharukov, I. Y.; Zaikovsky, V. I.; Kriventsov, V. V.; Parmon, V. N. Platinum Nanoparticles on Al_2O_3: Correlation between the Particle Size and Activity in Total Methane Oxidation. *J. Catal.* **2009**, *268*, 60−67.
(79) Hansen, T. K.; Høj, M.; Hansen, B. B.; Jensen, A. D.; Janssens, T. V. W. The Effect of Pt Particle Size on the Oxidation of CO, and NO Over Pt/Al_2O_3 for Diesel Exhaust Aftertreatment. *Top. Catal.* **2017**, *60*, 1333−1344.

https://dx.doi.org/10.1021/acsanm.0c02456
ACS Appl. Nano Mater. 2020, 3, 11352−11362